Author(s): Kurttila, Moona; Rumfeldt, Jessica; Takala, Heikki; Ihalainen, Janne A.

Title: The interconnecting hairpin extension "arm" : An essential allosteric element of phytochrome activity

Please cite the original version:

Kurttila, M., Rumfeldt, J., Takala, H., & Ihalainen, J. A. (2023). The interconnecting hairpin
extension "arm" : An essential allosteric element of phytochrome activity. Structure, 31(9),
1100-1108, e1-e4. https://doi.org/10.1016/j.str.2023.06.007

The interconnecting hairpin extension "arm": An essential allosteric element of phytochrome activity

Graphical abstract
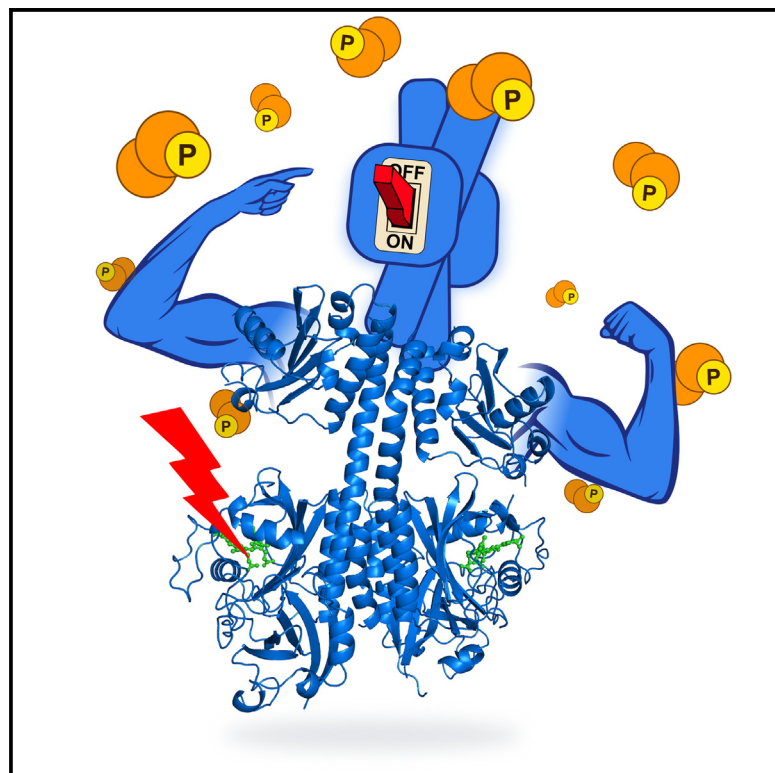
Authors

Moona Kurttila, Jessica Rumfeldt,
Heikki Takala, Janne A. Ihalainen

Correspondence

heikki.p.takala@jyu.fi (H.T.),
janne.ihalainen@jyu.fi (J.A.I.)

In brief

Kurttila et al. demonstrated that an interconnecting hairpin structure in the photosensory module of a red light photosensor phytochrome is crucial for controlling the activity of the system. For light activation, the hairpin allows signal transduction beyond the chromophore environment. In the resting state, the hairpin supports the structural stability.

Highlights

- Activity cannot be controlled by light without the hairpin extension in the sensory module

- Dark state chromophore environment is virtually unaffected upon removal of the hairpin

- Structure of a phytochrome photosensory module without the hairpin is reported

- The hairpin extension stabilizes the system, both thermally and kinetically

CellPress

Structure

Article

The interconnecting hairpin extension "arm": An essential allosteric element of phytochrome activity

Moona Kurttila,[1] Jessica Rumfeldt,[1] Heikki Takala,[1,*] and Janne A. Ihalainen[1,2,*]
[1]University of Jyvaskyla, Nanoscience Center, Department of Biological and Environmental Science, 40014 Jyvaskyla, Finland
[2]Lead contact
*Correspondence: heikki.p.takala@jyu.fi (H.T.), janne.ihalainen@jyu.fi (J.A.I.)
https://doi.org/10.1016/j.str.2023.06.007

SUMMARY

In red-light sensing phytochromes, isomerization of the bilin chromophore triggers structural and dynamic changes across multiple domains, ultimately leading to control of the output module (OPM) activity. In between, a hairpin structure, "arm", extends from an interconnecting domain to the chromophore region. Here, by removing this protein segment in a bacteriophytochrome from *Deinococcus radiodurans* (*Dr*BphP), we show that the arm is crucial for signal transduction. Crystallographic, spectroscopic, and biochemical data indicate that this variant maintains the properties of *Dr*BphP in the resting state. Spectroscopic data also reveal that the armless systems maintain the ability to respond to light. However, there is no subsequent regulation of OPM activity without the arms. Thermal denaturation reveals that the arms stabilize the *Dr*BphP structure. Our results underline the importance of the structurally flexible interconnecting hairpin extensions and describe their central role in the allosteric coupling of phytochromes.

INTRODUCTION

All living organisms use various sensory systems to adapt to their ambient environment. Phytochromes are red-light sensory proteins in plants, bacteria, and fungi. They photoswitch between two distinguishable states: a red-light absorbing Pr state and a far-red light-absorbing Pfr state (Figure 1A). Phytochromes are known to accommodate a variety of output modules (OPM) allowing them to participate in different developmental and regulatory events.[1] The OPM in bacterial phytochromes is often a histidine kinase (HK), rendering them as sensors in two-component signaling systems. The photosensory module (PSM) of the phytochrome superfamily is conserved, consisting of the chromophore binding domain (CBD) complemented by a phytochrome-specific (PHY) domain that structurally connects the CBD and OPM. In bacterial phytochromes, absorption of red light causes isomerization of a covalently bound biliverdin (BV) chromophore.[2–5] This perturbation in the chromophore-binding pocket, the allosteric site, triggers structural and dynamic changes in the protein moiety, which ultimately leads to allosteric regulation of the OPM activity at the functional site.[6,7]

Bacterial phytochromes share a highly similar PSM organization as most plant, fungal, and cyanobacterial phytochromes, regardless of their variety in effector modules.[8] Most of these systems include a structurally flexible PHY hairpin extension, often referred to as the "tongue", but in this study referred to as an "arm" (in green in Figure 1A).[9,10] It extends from the PHY domain core to the vicinity of the chromophore, forming highly conserved interactions with the GAF (cGMP phosphodiesterase-adenylate cyclase-FhlA) domain that together with PAS (Period-ARNT-Single-minded) forms the CBD.[11,12] These interactions are found even in PAS-less phytochromes, like cyanobacterial *Synechocystis* Cph2,[11] which speaks for their high conservation within phytochrome superfamily. From its other end, the arm is connected (via a short linker region and the PHY domain core) to a long helix that in bacterial systems extends to the output HK module.[11]

The arm brings intrinsic disorder into the phytochrome system as it fluctuates between multiple conformations. In the Pr state, the arm is mainly folded as a β-sheet, and during photoconversion to Pfr, it refolds into an α-helix (Figure 1A).[7,11–15] However, it has been demonstrated that the arm can fluctuate away from its interaction site at the GAF domain even in the Pr state.[15,16] Since the discovery of the arm's light-induced refolding,[12] much attention has been drawn to its structure and role in phytochrome signal transduction.[7,15–24] The arm connects the two other structural tiers of phytochrome, the chromophore binding pocket and the OPM.[1] Although signal transduction routes via the central helix have been suggested,[22,25] no clear and coherent view of the coupling between the three tiers has been reached yet.

To elucidate the allosteric coupling in phytochromes and the role of the arm in phytochrome signaling in a direct manner, we removed the arm extension from the full-length (FL) and PSM (CBD-PHY) fragments of *Deinococcus radiodurans* bacteriophytochrome (*Dr*BphP). With the deletion, we
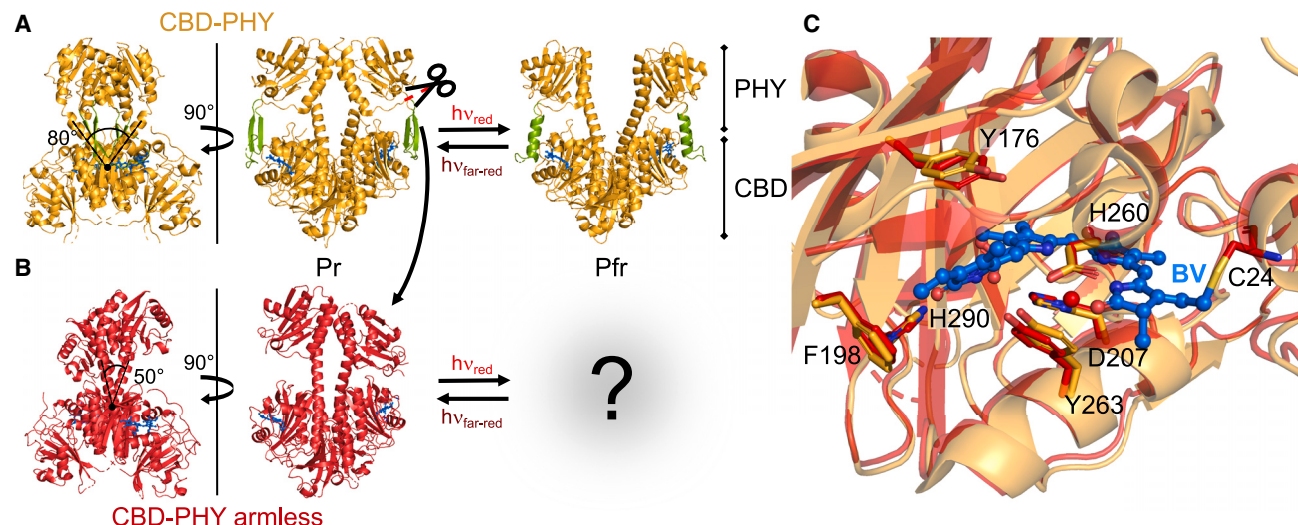
Structure
Article

Figure 1. The dark state crystal structure of the CBD-PHY armless

(A) Dark and illuminated crystal structures of CBD-PHY. The "arm" is colored in green, and the covalently bound biliverdin (BV) is shown as blue sticks buried inside the chromophore binding domain (CBD).

(B) Dark state structure of CBD-PHY armless. The removal of the arms results in loss of the PHY domain symmetry in the dimer and change in the characteristic dimerization angle of the helical spine, visible in the 90° rotated view.

(C) Comparison of the chromophore binding pocket of CBD-PHY armless (red) and CBD-PHY (yellow) in the dark crystal structures reveals that the organization of residues in the chromophore binding pocket is highly similar. Some of the amino acids crucial for the photocycle are shown in sticks. Only the BV of CBD-PHY armless structure is shown in ball-stick presentation (blue) for clarity. PDB codes: 4O0P (CBD-PHY Pr[12]), 5C5K (CDB-PHY Pfr[14]), and 8BOR (CBD-PHY armless).

created armless phytochrome variants with disrupted allosteric tiers. By combining structural data with biochemical activity assays and spectroscopic results, we show that without the arm, the dark state structure and properties are mostly unaffected and the chromophore environment remains responsive to light, yet the information from the chromophore and CBD cannot be relayed to the OPM activity upon illumination.

RESULTS

The dark state structure of armless photosensory module

The armless variants were created by clipping out the "arm" hairpin extension (segment between R446-G478) and by replacing it with a sequence "GGGS". The CBD-PHY armless variant crystallized as a parallel dimer, like the wild-type CBD-PHY construct, and the structure could be resolved up to 2.3 Å resolution (Figures 1 and S1, Table 1).[12,14] The overall structural features resemble those of its arm-containing counterpart, except the dimer symmetry is lost without the arms as the PHY domains appear tilted. One monomer of the PHY is docked against its corresponding CBD, while the other is pulled further from its CBD. The observed PHY domain positioning can be driven by crystal packing as it results in a smaller B-factor in the docked domain (Figure S2 A). This underlines the importance of the arms in stabilizing the orientation of the PHY domains. However, the removal of the arm did not affect the overall fold of the remaining PHY domain (Figure S2B).

Further differences between the wild-type and armless dark state structures can be found from the dimerization angle of the monomers, in the 90° rotated view in Figure 1. In the wild-

type, the angle between the interconnecting helices of the two monomers at the pivot point is about 80°, whereas in the armless it is only about 50°. This results in a slightly larger interface area between the two monomers in the CBD-PHY armless (Figure S2C). Despite the altered orientation, the CBD and PHY domains in both monomers have the same fold as in the wild-type. Comparison of the chromophore binding pockets of the dark state structures reveals that the organization of the residues is nearly the same (Figure 1C). Even the conserved residues Y263 and D207, which are responsible for the interaction network with the arm,[12] have configurations in the structures highly similar to wild-type.

The removal of arms results in CBD-like spectroscopic behavior

The switchability of the armless variants was confirmed with UV-vis spectroscopy (Figure 2A). The spectra reveal that both CBD-PHY armless and FL armless can be switched back and forth between the illuminated and dark states. The dark state spectra of all constructs are nearly identical, in line with the similar organization of the chromophore binding pockets (Figure 1C). The illuminated state spectra of the armless systems resemble that of CBD. The BV conformations and isomerization yields were further studied by the urea-denatured samples and their UV-vis absorption.[26] The urea-denatured Pr spectra of both armless systems reveal the BV to be in ZZZ conformation, identical to CBD-PHY and CBD (Figures S3A–S3C). The isomerization takes place in the armless systems upon illumination, but the ZZE yield is slightly lower in CBD and armless constructs than in the wild-type CBD-PHY (Figures S3D–S3F). After illumination, canonical phytochromes thermally revert back to the Pr

CellPress

OPEN ACCESS

Table 1. X-ray diffraction data collection and refinement statistics for the dark state (Pr) structure of CBD-PHY armless

Data Collection	
Space group	P 1 2₁ 1
Cell dimensions	
a, b, c (Å)	119.63, 64.59, 131.04
α, β, γ (°)	90.00, 91.55, 90.00
Resolution (Å)	50.00–2.30 (2.36–2.30)
R_{merge}	0.152 (1.496)
$CC_{1/2}$	0.989 (0.325)
I/σ(I)	5.40 (0.94)
Completeness (%)	98.8 (99.2)
Redundancy	3.29 (3.26)
Wilson B factor	45.1
Refinement	
Resolution (Å)	45.99–2.30 (2.36–2.30)
No. of reflections	83924 (6133)
R_{work}/R_{free}	0.235/0.268 (0.366/0.393)
No. of atoms	
Protein	14041
Ligand	172
Water	426
Overall B-factor (Å²)	53.0
Geometry	
RMSD	
Bond lengths (Å)	0.004
Bond angles (°)	0.989
Ramachandran	
Favored (%)	98.3
Allowed (%)	1.7
Outliers (%)	0
Clashscore	4.2

Figure 2. UV-vis and FTIR difference spectra show a CBD-like illuminated state for both armless constructs

(A) UV-vis spectra of the constructs show the difference in the biliverdin (BV) absorbance between dark (black lines) and illuminated (red lines) states.

(B) The FTIR difference spectra (Pfr *minus* Pr) of CBD-PHY armless and FL armless compared to the one of CBD. The spectral properties of both armless samples are nearly identical to CBD.

(C) In contrast, the spectral properties of wild-type CBD-PHY and FL are very different from CBD. All spectra are scaled to the BV signal at 1712 cm⁻¹.

state with a range of rates, depending on the construct.[27] The armless constructs revert back to the Pr state in tens of minutes, much faster compared to their wild-type counterparts, which have dark reversion rates of hours (Figure S4). The armless systems have a fast monophasic reversion. The inclusion of arms results in a second slow component, with a time constant of hours (Figure S4B).

The light-induced changes in BV and protein moiety interactions were studied by recording FTIR difference spectra between the illuminated and dark states (Figures 2B and 2C). Similar to UV-vis spectroscopy, the FTIR difference signals of both CBD-PHY armless and FL armless strongly resemble those of CBD. The negative BV signals at 1736 cm⁻¹ and 1712 cm⁻¹, are due to the disappearance of the A-ring and D-ring carbonyl interactions, respectively, which is a result of BV isomerization, as observed also in wild-type CBD-PHY and FL (Figure 2C).[19,28] In all systems, the H-bond network strength of the D-ring carbonyl increases from Pr to Pfr, observed as a frequency shift to lower energy. The large symmetric band at 1685 cm⁻¹ observed in CBD-PHY and FL reveals the H-bond network between the C=O group of the BV and H201 and S468 sites in
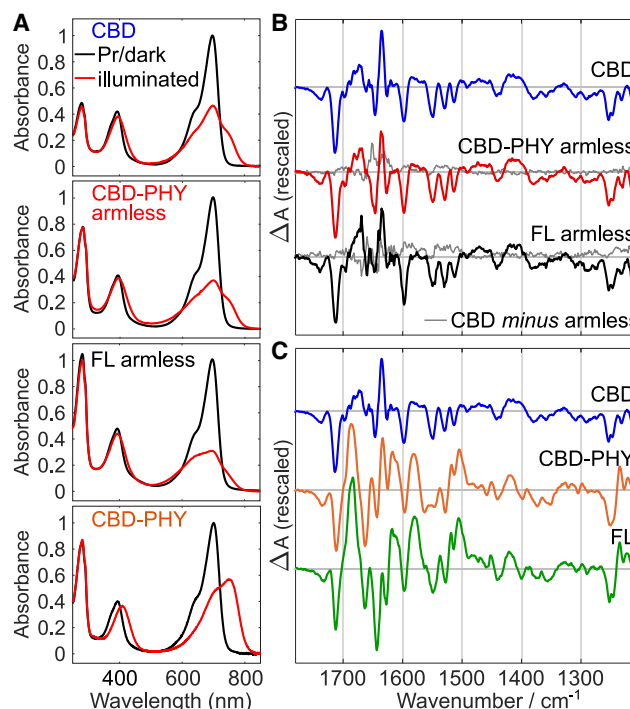
Pfr.[28] In CBD, as well as in the armless constructs, the positive contribution of the BV C=O vibration is wider. In isotope-labeled CBD, where the shifted amide I signals do not disturb this region, the band continues up to 1620 cm⁻¹ (Figure S5A). This indicates that the H-bonding strength varies on a wider scale than in arm-containing samples.[18] Comparison between isotope-labeled and non-isotope-labeled CBD indicates further signals from BV, located around 1250–1200 cm⁻¹ (Figure S5A). While the peaks in this region are remarkably similar between CBD and the armless constructs, they differ from CBD-PHY and FL by having notably larger positive contributions, again suggesting differences in the illuminated state BV environment (Figure 2C).

The differences in the FTIR signals between the isotope-labeled and non-isotope-labeled CBD indicate that, in addition to the chromophore changes, illumination results in changes within the protein moiety (Figure S5A). The amide I signals (C=O stretching vibration in the peptide bond) shift typically 40–50 cm⁻¹ and amide II signals (a mixed vibration of N-H bending and C-N stretching) shift about 30 cm⁻¹ due to the ¹³C¹⁵N-isotopes in the amino acids.[29,30] A negative-negative-positive peak pattern (1660 (−), 1645 (−), 1634 (+) cm⁻¹) was differentiated in CBD and isotope-labeled CBD with a 42–44 cm⁻¹ shift (Figure S5A). This correlates with an increase in turns and disordered structure in Pr, and increased β-sheet
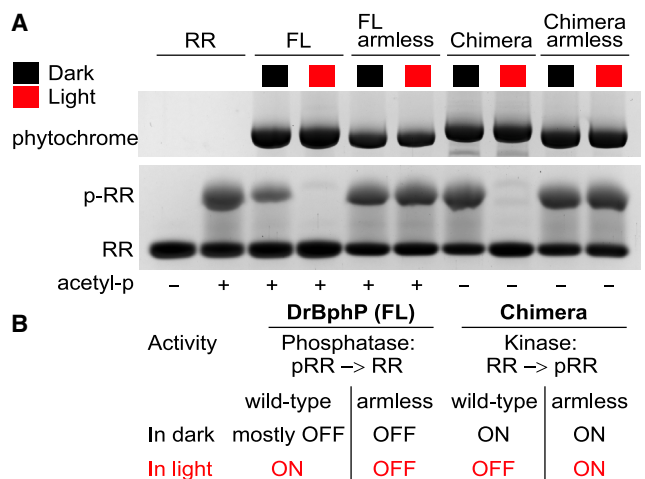
A

B

Activity	**DrBphP (FL)**		**Chimera**	
	Phosphatase: pRR –> RR		Kinase: RR –> pRR	
	wild-type	armless	wild-type	armless
In dark	mostly OFF	OFF	ON	ON
In light	ON	OFF	OFF	ON

Figure 3. The light control of the OPM enzymatic activity is lost upon arm removal
(A) PhosTag gel shows the amount of phosphorylated response regulator (p-RR), which is dependent on the OPM activity as well as the light conditions.
(B) Interpretation of the gel. FL construct has phosphatase activity under red light illumination, which is detected as diminished p-RR band under red light. In FL armless, the p-RR amount remains unaltered regardless of illumination. Chimera shows net kinase activity in dark, which is visible as an increase of p-RR content. Once the arm is removed in Chimera armless, its kinase activity remains unaffected by red light.

content in Pfr.[29] A similar FTIR signal pattern can also be found in the CBD-PHY and FL systems (Figure 2).[18,24] Indeed, in the Pr and Pfr state crystal structures, a slight light-induced increase in β-sheet structure is observed in the CBD region (Figure S5B).[12,14] However, direct correlation of the FTIR signals with the structural changes observed in crystallography would require site-selective isotope labeling. Naturally, the amide I region differs between CBD-PHY and FL in comparison to CBD and armless systems, indicating further protein moiety changes in the arm-containing systems. The refolding of the arm hairpin under study affects this region in both CBD-PHY and FL.[19,24] Therefore, pinpointing FTIR signals which originate from the light-induced changes in the OPM[7] is to be addressed in future studies. To conclude, no distinguishable light-induced structural changes outside the CBD are observed in the armless constructs.

Arm removal locks biochemical activity

DrBphP is shown to act as a light-activated phosphatase that dephosphorylates its cognate response regulator (DrRR) under red light.[31] Here, the phosphatase activity of the FL armless was studied in the dark and under saturating red light. The light-induced and uninduced reactions were run on a PhosTag gels, which allows distinguishing phosphorylated proteins from their unphosphorylated counterparts based on their lower mobility in the gel matrix (Figure 3A). The amount of phosphorylated RR (p-RR) was not reduced when incubated with FL armless under red light, which indicates that the phosphatase activity is not switched on, unlike in the case of FL wild-type. The (in)activity remained very similar despite the light state, and therefore the FL armless activity has a close to 1-fold dynamic range describing the magnitude of change in activity be-

tween the two states.[24] Comparison to the p-RR lane alone shows that, whereas FL has a little bit of activity even in the dark state, in FL armless it is constantly inactive. Like FL armless, the apoprotein of DrBphP remains inactive regardless of illumination condition (Figure S6D).

To test the possibility that the lack of light-induced activity is due to the disruption of the OPM functionality in the armless system, we analyzed a phytochrome "Chimera" variant, first introduced in Multamäki et al.[31] The Chimera consists of a PSM from DrBphP, and an output HK module from Agrobacterium tumefaciens phytochrome Agp1. Unlike DrBphP, the chimera acts as an HK that phosphorylates its cognate RR in the dark but lacks net kinase activity under red light (Figure 3B).[31,32] In the Chimera, the phosphorylation activity is observed through the appearance of a p-RR band in dark, while under red light, only a non-phosphorylated RR band is detected, indicating that the net kinase activity is turned off (Figure 3). In the Chimera armless, a p-RR band is observed in the dark as well as under red light, indicating that the protein has kinase activity in both states and therefore has lost the ability to respond to red light. Hence, the phytochrome OPM remains functional but not controllable without the arm. The full gel of the assay and repeats are shown in Figures S6A–S6C.

Interplay between the arm and OPM affects thermal stability

Circular dichroism (CD) spectroscopy was applied to study the thermal stability of our phytochrome systems. Temperature-induced denaturation was detected at two different wavelengths, at far-UV region (222 nm) and at near-UV region (281 nm), revealing changes in secondary and tertiary structures, respectively.[33] Denaturation experiments with dimeric, multidomain proteins are often complex due to protein concentration dependence of dissociation, multiple transition temperatures and increased misfolding and aggregation propensity relative to single domain proteins.[34–36] In our systems, unfolding is concomitant with irreversible aggregation and/or conformational lock, hampering a thermodynamic equilibrium analysis; the change in free energy, enthalpy, or entropy upon unfolding cannot, therefore, be determined. Instead, we used the fitted melting temperatures (T_m, Equations 1–3) as an approximation of the stability of our protein complexes in dark and illuminated states. In all studied constructs, two separate T_ms were observed: one at 41–65°C and another at 72–77°C (Figure 4). In the case of 222 nm detection, a single transition is observed in all cases. With 281 nm detection, two transitions, with decreasing and increasing signals, are observed in CBD-PHY and FL, while only one is observed in the armless systems.

To investigate the origin of the two T_ms, we also tracked the UV-vis absorbance of BV at 700 nm as a function of temperature in the dark state (Figure S7). The 700 nm signal decreased as a function of temperature due to the denaturation of the BV environment. A T_m of about 72°C was observed for both CBD and CBD-PHY (Figure S7). Further, for the CBD fragment, a T_m of over 74°C was detected at both CD detection wavelengths (Figures S8A and S8C). These observations indicate that the CBD has the highest T_m of the three subunits. Its structure is strongly stabilized by the chromophore binding, as lack of BV decreases the T_m by nearly 30°C (Figure S8). The capability to

Structure
Article
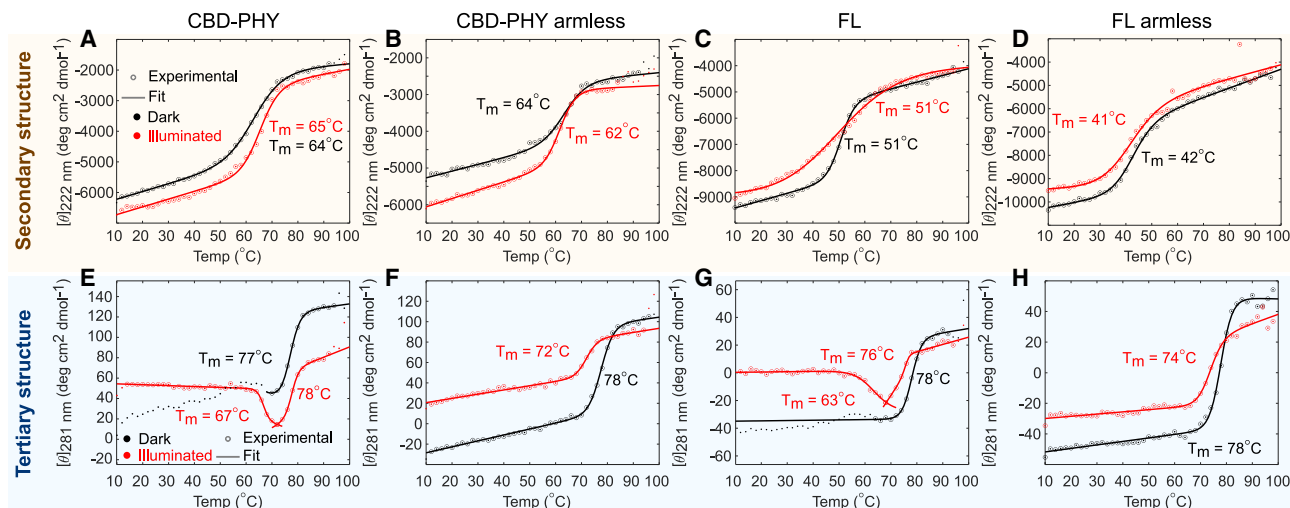
CellPress
OPEN ACCESS

Figure 4. Thermograms of CBD-PHY, CBD-PHY armless, FL, and FL armless at 222 nm and 281 nm in dark and illuminated states
(A–D) Denaturation monitored as ellipticity at 222 nm (dots) in dark (black) and illuminated (red) states. The fits according to Equation 3 are shown as solid lines. (E–H) Denaturation monitored as ellipticity at 281 nm in dark and illuminated states. The illuminated states of CBD-PHY and FL have two transitions, and both fits are shown. The T_m values obtained from the fits are marked next to the corresponding plots.

detect this transition with a near-UV CD signal can be rationalized from a structural point of view. The temperature-dependent signal at 281 nm mainly relates to the exposure of the aromatic amino acids in the hydrophobic pockets. In phytochromes, the most globular structure containing hydrophobic pockets is the CBD with its chromophore-binding cleft.

The lower T_ms in CBD-PHY and FL at around 64–65 and 51°C are observed at 222 nm, and are associated with denaturation of the PHY and PHY-HK modules, respectively. Confirmed by measuring the CBD-PHY melting profiles at 222 nm in three different concentrations, these transitions are not related to monomerization as a higher concentration resulted in lower T_m with a smaller change in the signal intensity (Figure S9C).[36] Rather, the observation indicates that the PHY and PHY-HK modules denature in an irreversible manner and therefore earlier at higher concentrations. The denaturation profile is also affected by the heating rate. Slower heating rate resulted in a lower T_m, due to increased time for aggregation at lower temperatures (Figure S9D).[34]

In CBD-PHY armless, the fitted T_ms tracked from secondary (64°C) and tertiary structures (78°C) are nearly identical to CBD-PHY (Figures 4B and 4F). In the dark state, the arm does not seem to affect the structural stability of the CBD-PHY construct. However, in the illuminated state, differences between the wild-type and armless constructs become apparent. In CBD-PHY, the T_ms of both PHY and CBD domains increased by 1°C (Figures 4A and 4E), whereas in CBD-PHY armless, both T_ms decreased in comparison to the dark state values (Figures 4B and 4F), which reflects decreased structural stability.

In the illuminated state of CBD-PHY, two separate transitions, decreasing and increasing signals, respectively, in the 281 nm thermogram are observed. The T_m of 67°C is observed as a decreasing CD signal, and Figure S9B reveals that the blue end of the BV Soret absorption (300–470 nm) affects this signal at the same temperature range. Especially in the illuminated state, the arm shifts the Soret band (Figure S9B), and melting

of the PHY domain (including the arm) changes the BV absorption, which reflects to the 281 nm signal. This effect is also observed in FL as a T_m of 63°C (Figure 4G). This suggests that the "dip" in the signal originates from the melting of the arm with subsequent changes in the BV environment. Therefore, the decreasing signals are naturally absent in the armless variants (Figures 4F and 4H).

When comparing the denaturation of the PHY-HK units, the T_m of FL armless is notably lower than that of wild-type FL, even in the dark state (Figures 4C, 4D, 4G, and 4H). Again in the armless, the T_ms decrease in the illuminated state in comparison to the dark. In FL wild-type, the fitted T_ms in dark and illuminated states were the same, 51°C. However, in the illuminated state the shape of the denaturation curve is more shallow than others, suggesting multiple overlapping transitions. In both FL systems, the T_m of the CBD part in the dark (78°C) is nearly identical to other constructs (Figures 4G and 4H). In FL, the T_m of the CBD part decreases to 76°C in the illuminated state.

DISCUSSION

The stability and activity of multidomain protein complexes can be regulated in different ways. Subtle changes in the protein fold can lead to dramatic effects on the characteristics of large protein complexes.[7,36,37] Typically in the allostery of multidomain signaling proteins, a connecting domain transmits a signal from the regulatory site to the functional site.[37,38] In phytochromes, the PHY domain structurally and functionally links the photoactivating CBD and the biochemically active OPM. Here, we demonstrated that the arm, a dynamic hairpin structure in the PHY domain, plays a crucial role in the (de)activation of the OPM. In Pr, with the methods used here, the lack of arm did not seem to affect the chromophore binding pocket. However, two different H-bonding environments of the D-ring have been observed previously,[39,40] which in principle can result from the
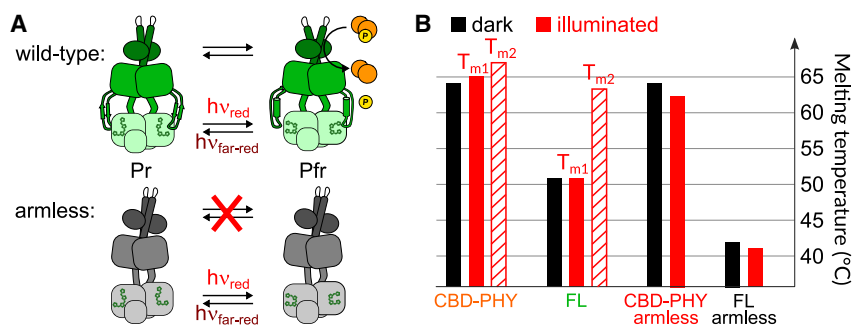
Figure 5. Phytochrome allostery

(A) Wild-type *Dr*BphP acts as a phosphatase, and its activity is switched on under red light. In the armless system, the chromophore and surrounding protein moiety remain responsive to light, as observed by FTIR and UV-vis spectroscopy, yet the activity of the OPM cannot be controlled by light.

(B) The thermal stability of CBD-PHY, FL, CBD-PHY armless, and FL armless systems represented by the T_m values of their PHY or PHY-HK unit in dark and illuminated states from Figures 4A–4D. The wild-type systems have an additional melting temperature (T_{m2}) that originates most probably from the melting of the arm and is detected as a decrease of the 281 nm signal (Figures 4E and 4G).

arm fluctuations. We showed that the arms are needed to stabilize the light-activated Pfr state of the chromophore. One suggestion is that this happens through dipole coupling between the α-helical arm and BV.[41] Further, the arm stabilizes the overall structure of the system and couples together, not only BV in the chromophore binding pocket and biochemically active OPM but also the three subunits in terms of thermal stability, making it a key element in phytochrome allostery (Figure 5).

The dynamic range of a system describes how efficiently the enzymatic activity is altered in response to a signal.[42] It depends on the magnitude of the equilibrium shift between the active and inactive conformations and therefore high dynamic range requires strong coupling of the perturbation and functional sites.[38] We have previously described 33-fold dynamic range for *Dr*BphP activity.[24] Here, we showed that the armless systems had no significant difference in activity between dark and illuminated states (close to 1-fold dynamic range), and the coupling between the light-sensing (BV) and the functional site (OPM) is completely disrupted upon arm removal. Gourinchas et al. had similar results with an armless variant of *Is*PadC (*Is*PadC $\Delta^{442-477}$SG), a bacterial phytochrome with diguanylyl cyclase activity.[22] The wild-type *Is*PadC is activated under red light illumination and has a 43-fold dynamic range. The armless variant became continuously active and had larger maximal activity than its wild-type counterpart, with 1.6-fold repression of activity upon illumination.[22] Gourinchas et al. as well as Isaksson et al. have previously concluded that the helical spine acts as a signal transduction route between BV and the OPM.[22,25] The armless variants, however, demonstrate that the helical spine on its own cannot transduce the signal and that the arms are required for allosteric control of the OPM activity (Figure 5A).

The OPM of *Dr*BphP appears very dynamic,[7] which is in accord with the thermal stability of the PHY-OPM region. The T_m of the PHY-OPM subunits in FL is over 10°C lower than the T_m of the PHY domain alone in both CBD-PHY and CBD-PHY armless (Figure 5B). In this regard, the role of the arm becomes clear in the FL systems where dimeric interactions among the OPMs take place.[7,43] Without the arm, the thermal stability of the PHY and the OPM decreases significantly (Figure 5B). Further, the FL has a multi-phasic denaturation curve of the illuminated state, not observed in other systems (Figures 4A–4D), which reflects increased dynamics in the OPM[7] that take place hand-in-hand with the refolded arm. In the wild-type systems, the melting of the arm can be observed as a separate melting temperature (T_{m2} in Figure 5B). The arm and the OPM are struc-

turally and functionally coupled, but as the OPM and PHY domain denature hand-in-hand, also the core region of the PHY domain is closely coupled to the OPM.

Hairpin extensions and loops are known to be important allosteric mediators in multiple signaling systems.[44,45] Here, we revealed information regarding phytochrome allostery at multiple levels including atomic coordinates in the crystal structure, changes in intramolecular interactions probed by FTIR, changes in control of biochemical activity, and in thermal stability using temperature and illumination dependent CD spectroscopy. Our study indicates the role of the arm in phytochromes is particularly important for the light-activated state formation, stabilization, and regulation of phosphatase and kinase activity. In the resting state, the arm does not seem to affect the chromophore pocket organization. Despite its dynamic nature, the arm plays a role in maintaining overall structural stability and domain arrangement.[46] Upon illumination, the chromophore and CBD can switch to the light-activated state without the arm, but only the arm allows the signal transduction all the way to the OPM. The arm is therefore crucial for the allosteric coupling of the sensory and effector modules.

STAR★METHODS

Detailed methods are provided in the online version of this paper and include the following:

- KEY RESOURCES TABLE
- RESOURCE AVAILABILITY
  - Lead contact
  - Materials availability
  - Data and code availability
- EXPERIMENTAL MODEL AND STUDY PARTICIPANT DETAILS
- METHOD DETAILS
  - Cloning and DNA material
  - Protein expression and purification
  - Crystallography
  - Protein phosphorylation by acetyl phosphate and PhosTag detection
  - Spectroscopic measurements
  - UV-vis absorption spectroscopy
  - FTIR spectroscopy
  - CD spectroscopy
- QUANTIFICATION AND STATISTICAL ANALYSIS

Structure
Article

CellPress
OPEN ACCESS

- ○ Crystallographic data analysis
- ○ Spectroscopic data analysis

SUPPLEMENTAL INFORMATION

ACKNOWLEDGMENTS

AUTHOR CONTRIBUTIONS

M.K., H.T., and J.A.I. designed research; M.K., J.R., and H.T. performed research and analyzed data; and M.K. and J.A.I. wrote the paper with input from all other authors.

DECLARATION OF INTERESTS

The authors declare no competing interests.

INCLUSION AND DIVERSITY

We support inclusive, diverse, and equitable conduct of research.

REFERENCES

1. Takala, H., Edlund, P., Ihalainen, J.A., and Westenhoff, S. (2020). Tips and turns of bacteriophytochrome photoactivation. Photochem. Photobiol. Sci. 19, 1488–1510. https://doi.org/10.1039/D0PP00117A.

2. Kneip, C., Hildebrandt, P., Schlamann, W., Braslavsky, S.E., Mark, F., and Schaffner, K. (1999). Protonation state and structural changes of the tetrapyrrole chromophore during the Pr →Pfr phototransformation of phytochrome: a resonance raman spectroscopic study. Biochemistry 38, 15185–15192. pMID: 10563801. https://doi.org/10.1021/bi990688w.

3. Mroginski, M.A., Murgida, D.H., von Stetten, D., Kneip, C., Mark, F., and Hildebrandt, P. (2004). Determination of the Chromophore Structures in the Photoinduced Reaction Cycle of Phytochrome. J. Am. Chem. Soc. 126, 16734–16735. https://doi.org/10.1021/ja043959l.

4. van Thor, J.J., Mackeen, M., Kuprov, I., Dwek, R.A., and Wormald, M.R. (2006). Chromophore Structure in the Photocycle of the Cyanobacterial Phytochrome Cph1. Biophys. J. 91, 1811–1822. https://doi.org/10.1529/biophysj.106.084335.

5. Burgie, E.S., Wang, T., Bussell, A.N., Walker, J.M., Li, H., and Vierstra, R.D. (2014). Crystallographic and electron microscopic analyses of a bacterial phytochrome reveal local and global rearrangements during photoconversion. J. Biol. Chem. 289, 24573–24587. https://doi.org/10.1074/jbc.M114.571661.

6. Nussinov, R., and Tsai, C.-J. (2013). Allostery in Disease and in Drug Discovery. Cell 153, 293–305. https://doi.org/10.1016/j.cell.2013.03.034.

7. Wahlgren, W.Y., Claesson, E., Tuure, I., Trillo-Muyo, S., Bódizs, S., Ihalainen, J.A., Takala, H., and Westenhoff, S. (2022). Structural mechanism of signal transduction in a phytochrome histidine kinase. Nat. Commun. 13, 7673. https://doi.org/10.1038/s41467-022-34893-3.

8. Rockwell, N.C., and Lagarias, J.C. (2020). Phytochrome evolution in 3D: deletion, duplication, and diversification. New Phytol. 225, 2283–2300. https://doi.org/10.1111/nph.16240.

9. Essen, L.-O., Mailliet, J., and Hughes, J. (2008). The structure of a complete phytochrome sensory module in the Pr ground state. Proc. Natl. Acad. Sci. USA 105, 14709–14714. https://doi.org/10.1073/pnas.0806477105.

10. Yang, X., Kuk, J., and Moffat, K. (2008). Crystal structure of Pseudomonas aeruginosa bacteriophytochrome: Photoconversion and signal transduction. Proc. Natl. Acad. Sci. USA 105, 14715–14720. https://doi.org/10.1073/pnas.0806718105.

11. Anders, K., Daminelli-Widany, G., Mroginski, M.A., von Stetten, D., and Essen, L.-O. (2013). Structure of the Cyanobacterial Phytochrome 2 Photosensor Implies a Tryptophan Switch for Phytochrome Signaling. J. Biol. Chem. 288, 35714–35725. https://doi.org/10.1074/jbc.M113.510461.

12. Takala, H., Björling, A., Berntsson, O., Lehtivuori, H., Niebling, S., Hoernke, M., Kosheleva, I., Henning, R., Menzel, A., Ihalainen, J.A., and Westenhoff, S. (2014). Signal amplification and transduction in phytochrome photosensors. Nature 509, 245–248. https://doi.org/10.1038/nature13310.

13. Yang, X., Stojković, E.A., Ozarowski, W.B., Kuk, J., Davydova, E., and Moffat, K. (2015). Light Signaling Mechanism of Two Tandem Bacteriophytochromes. Structure 23, 1179–1189. https://doi.org/10.1016/j.str.2015.04.022.

14. Burgie, E.S., Zhang, J., and Vierstra, R.D. (2016). Crystal structure of Deinococcus phytochrome in the photoactivated state reveals a cascade of structural rearrangements during photoconversion. Structure 24, 448–457. https://doi.org/10.1016/j.str.2016.01.001.

15. Gustavsson, E., Isaksson, L., Persson, C., Mayzel, M., Brath, U., Vrhovac, L., Ihalainen, J.A., Karlsson, B.G., Orekhov, V., and Westenhoff, S. (2020). Modulation of Structural Heterogeneity Controls Phytochrome Photoswitching. Biophys. J. 118, 415–421. https://doi.org/10.1016/j.bpj.2019.11.025.

16. Rumfeldt, J.A., Kurttila, M., Takala, H., and Ihalainen, J.A. (2021). The hairpin extension controls solvent access to chromophore binding pocket in bacterial phytochrome – a UV-Vis absorption spectroscopy study. Photochem. Photobiol. Sci. 20, 117–1181. https://doi.org/10.1007/s43630-021-00090-2.

17. Otero, L.H., Klinke, S., Rinaldi, J., Velázquez-Escobar, F., Mroginski, M.A., Fernández López, M., Malamud, F., Vojnov, A.A., Hildebrandt, P., Goldbaum, F.A., and Bonomi, H.R. (2016). Structure of the Full-Length Bacteriophytochrome from the Plant Pathogen Xanthomonas campestris Provides Clues to its Long-Range Signaling Mechanism. J. Mol. Biol. 428, 3702–3720. https://doi.org/10.1016/j.jmb.2016.04.012.

18. Takala, H., Lehtivuori, H.K., Berntsson, O., Hughes, A., Nanekar, R., Niebling, S., Panman, M., Henry, L., Menzel, A., Westenhoff, S., and Ihalainen, J.A. (2018). On the (un)coupling of the chromophore, tongue interactions, and overall conformation in a bacterial phytochrome. J. Biol. Chem. 293, 8161–8172. https://doi.org/10.1074/jbc.RA118.001794.

19. Stojković, E.A., Toh, K.C., Alexandre, M.T.A., Baclayon, M., Moffat, K., and Kennis, J.T.M. (2014). FTIR Spectroscopy Revealing Light-Dependent Refolding of the Conserved Tongue Region of Bacteriophytochrome. J. Phys. Chem. Lett. 15, 2512–2515. https://doi.org/10.1021/jz501189t.

20. Björling, A., Berntsson, O., Lehtivuori, H., Takala, H., Hughes, A.J., Panman, M., Hoernke, M., Niebling, S., Henry, L., Henning, R., et al. (2016). Structural photoactivation of a full-length bacterial phytochrome. Sci. Adv. 2, e1600920. https://doi.org/10.1126/sciadv.1600920.

21. Anders, K., Gutt, A., Gärtner, W., and Essen, L.-O. (2014). Phototransformation of the red light sensor cyanobacterial phytochrome 2 from Synechocystis species depends on its tongue motifs. J. Biol. Chem. 289, 25590–25600. https://doi.org/10.1074/jbc.m114.562082.

CellPress
OPEN ACCESS

Structure
Article

22. Gourinchas, G., Etzl, S., Göbl, C., Vide, U., Madl, T., and Winkler, A. (2017). Long-range allosteric signaling in red light-regulated diguanylyl cyclases. Sci. Adv. *3*, e1602498. https://doi.org/10.1126/sciadv.1602498.

23. Gourinchas, G., Heintz, U., and Winkler, A. (2018). Asymmetric activation mechanism of a homodimeric red light-regulated photoreceptor. Elife *7*, e34815. https://doi.org/10.7554/eLife.34815.

24. Kurttila, M., Etzl, S., Rumfeldt, J., Takala, H., Galler, N., Winkler, A., and Ihalainen, J.A. (2022). The structural effect between the output module and chromophore-binding domain is a two-way street via the hairpin extension. Photochem. Photobiol. Sci. *21*, 1881–1894. https://doi.org/10.1007/s43630-022-00265-5, ISSN 1474-9092.

25. Isaksson, L., Gustavsson, E., Persson, C., Brath, U., Vrhovac, L., Karlsson, G., Orekhov, V., and Westenhoff, S. (2021). Signaling Mechanism of Phytochromes in Solution. Structure *29*, 151–160.e3. https://doi.org/10.1016/j.str.2020.08.009.

26. Lehtivuori, H., Rumfeldt, J., Mustalahti, S., Kurkinen, S., and Takala, H. (2022). Conserved histidine and tyrosine determine spectral responses through the water network in *Deinococcus radiodurans* phytochrome. Photochem. Photobiol. Sci. *21*, 1975–1989. https://doi.org/10.1007/S43630-022-00272-6/TABLES/3, ISSN 14749092.

27. Takala, H., Lehtivuori, H., Hammarén, H., Hytönen, V.P., and Ihalainen, J.A. (2014). Connection between absorption properties and conformational changes in *Deinococcus radiodurans* phytochrome. Biochemistry *53*, 7076–7085. https://doi.org/10.1021/bi501180s.

28. Ihalainen, J.A., Gustavsson, E., Schroeder, L., Donnini, S., Lehtivuori, H., Isaksson, L., Thöing, C., Modi, V., Berntsson, O., Stucki-Buchli, B., et al. (2018). Chromophore-protein interplay during the phytochrome photocycle revealed by step-scan FTIR spectroscopy. J. Am. Chem. Soc. *140*, 12396–12404. https://doi.org/10.1021/jacs.8b04659.

29. Barth, A. (2007). Infrared spectroscopy of proteins. Biochim. Biophys. Acta *1767*, 1073–1101. https://doi.org/10.1016/j.bbabio.2007.06.004.

30. Brielle, E.S., and Arkin, I.T. (2021). Isotope-Edited Amide II Mode: A New Label for Site-Specific Vibrational Spectroscopy. J. Phys. Chem. Lett. *12*, 6634–6638. pMID: 34254809. https://doi.org/10.1021/acs.jpclett.1c01073.

31. Multamäki, E., Nanekar, R., Morozov, D., Lievonen, T., Golonka, D., Wahlgren, W.Y., Stucki-Buchli, B., Rossi, J., Hytönen, V.P., Westenhoff, S., et al. (2021). Comparative analysis of two paradigm bacteriophytochromes reveals opposite functionalities in two-component signaling. Nat. Commun. *12*, 4394. https://doi.org/10.1038/s41467-021-24676-7.

32. Lamparter, T., Michael, N., Mittmann, F., and Esteban, B. (2002). Phytochrome from *Agrobacterium tumefaciens* has unusual spectral properties and reveals an N-terminal chromophore attachment site. Proc. Natl. Acad. Sci. USA *99*, 11628–11633. https://doi.org/10.1073/pnas.152263999.

33. Greenfield, N.J. (2006). Using circular dichroism collected as a function of temperature to determine the thermodynamics of protein unfolding and binding interactions. Nat. Protoc. *1*, 2527–2535. https://doi.org/10.1038/nprot.2006.204.

34. Vermeer, A.W., and Norde, W. (2000). The Thermal Stability of Immunoglobulin: Unfolding and Aggregation of a Multi-Domain Protein. Biophys. J. *78*, 394–404. https://doi.org/10.1016/S0006-3495(00)76602-1.

35. Rumfeldt, J.A.O., Stathopulos, P.B., Chakrabarrty, A., Lepock, J.R., and Meiering, E.M. (2006). Mechanism and Thermodynamics of Guanidinium Chloride-induced Denaturation of ALS-associated Mutant Cu,Zn Superoxide Dismutases. J. Mol. Biol. *355*, 106–123. https://doi.org/10.1016/j.jmb.2005.10.042.

36. Doyle, C.M., Rumfeldt, J.A., Broom, H.R., Broom, A., Stathopulos, P.B., Vassall, K.A., Almey, J.J., and Meiering, E.M. (2013). Energetics of oligomeric protein folding and association. Arch. Biochem. Biophys. *531*, 44–64. https://doi.org/10.1016/j.abb.2012.12.005.

37. Mensa, B., Polizzi, N.F., Molnar, K.S., Natale, A.M., Lemmin, T., and DeGrado, W.F. (2021). Allosteric mechanism of signal transduction in the two-component system histidine kinase PhoQ. Elife *10*, e73336. https://doi.org/10.7554/eLife.73336, ISSN 2050-084X.

38. Tsai, C.-J., and Nussinov, R. (2014). A Unified View of "How Allostery Works". PLoS Comput. Biol. *10*, 1–12. https://doi.org/10.1371/journal.pcbi.1003394.

39. Song, C., Psakis, G., Lang, C., Mailliet, J., Gärtner, W., Hughes, J., Matysik, J., and Lagarias, C.J. (2011). Two ground state isoforms and a chromophore D-ring photoflip triggering extensive intramolecular changes in a canonical phytochrome. Proc. Natl. Acad. Sci. USA *108*, 3842–3847. https://doi.org/10.1073/pnas.1013377108.

40. Chenchiliyan, M., Kübel, J., Ooi, S.A., Salvadori, G., Mennucci, B., Westenhoff, S., and Maj, M. (2023). Ground-state heterogeneity and vibrational energy redistribution in bacterial phytochrome observed with femtosecond 2D IR spectroscopy. J. Chem. Phys. *158*, 10897690. https://doi.org/10.1063/5.0135268.

41. Buhrke, D., Michael, N., and Hamm, P. (2022). Vibrational couplings between protein and cofactor in bacterial phytochrome Agp1 revealed by 2D-IR spectroscopy. Proc. Natl. Acad. Sci. USA *119*, e2206400119. https://doi.org/10.1073/PNAS.2206400119.

42. Ziegler, T., and Möglich, A. (2015). Photoreceptor engineering. Front. Mol. Biosci. *2*, 30. https://doi.org/10.3389/fmolb.2015.00030.

43. Takala, H., Björling, A., Linna, M., Westenhoff, S., and Ihalainen, J.A. (2015). Light-induced Changes in the Dimerization Interface of Bacteriophytochromes. J. Biol. Chem. *290*, 16383–16392. https://doi.org/10.1074/jbc.M115.650127.

44. Gora, A., Brezovsky, J., and Damborsky, J. (2013). Gates of Enzymes. Chem. Rev. *113*, 5871–5923. https://doi.org/10.1021/cr300384w.

45. Ho, K., and Bradshaw, N. (2021). A conserved allosteric element controls specificity and activity of functionally divergent PP2C phosphatases from *Bacillus subtilis*. J. Biol. Chem. *296*, 100518. https://doi.org/10.1016/j.jbc.2021.100518.

46. Motlagh, H.N., Wrabl, J.O., Li, J., and Hilser, V.J. (2014). The ensemble nature of allostery. Nature *508*, 331–339. https://doi.org/10.1038/nature13001.

47. Wagner, J.R., Brunzelle, J.S., Forest, K.T., and Vierstra, R.D. (2005). A light-sensing knot revealed by the structure of the chromophore-binding domain of phytochrome. Nature *438*, 325–331. https://doi.org/10.1038/nature04118.

48. Wagner, J.R., Zhang, J., Brunzelle, J.S., Vierstra, R.D., and Forest, K.T. (2007). High resolution structure of *Deinococcus* bacteriophytochrome yields new insights into phytochrome architecture and evolution. J. Biol. Chem. *282*, 12298–12309. https://doi.org/10.1074/jbc.M611824200.

49. Wagner, J.R., Zhang, J., von Stetten, D., Günther, M., Murgida, D.H., Mroginski, M.A., Walker, J.M., Forest, K.T., Hildebrandt, P., and Vierstra, R.D. (2008). Mutational analysis of *Deinococcus radiodurans* bacteriophytochrome reveals key amino acids necessary for the photochromicity and proton exchange cycle of phytochromes. J. Biol. Chem. *283*, 12212–12226. https://doi.org/10.1074/jbc.M709355200.

50. Kabsch, W. (1993). Automatic processing of rotation diffraction data from crystals of initially unknown symmetry and cell constants. J. Appl. Crystallogr. *26*, 795–800. https://doi.org/10.1107/S0021889893005588.

51. McCoy, A.J., Grosse-Kunstleve, R.W., Adams, P.D., Winn, M.D., Storoni, L.C., and Read, R.J. (2007). *Phaser* crystallographic software. J. Appl. Crystallogr. *40*, 658–674. https://doi.org/10.1107/S0021889807021206.

52. Emsley, P., and Cowtan, K. (2004). *Coot*: model-building tools for molecular graphics. Acta Crystallogr. D *60*, 2126–2132. https://doi.org/10.1107/S0907444904019158.

53. Murshudov, G.N., Skubák, P., Lebedev, A.A., Pannu, N.S., Steiner, R.A., Nicholls, R.A., Winn, M.D., Long, F., and Vagin, A.A. (2011). *REFMAC*5 for the refinement of macromolecular crystal structures. Acta Crystallogr. D *67*, 355–367. https://doi.org/10.1107/S0907444911001314.

54. Winn, M.D., Ballard, C.C., Cowtan, K.D., Dodson, E.J., Emsley, P., Evans, P.R., Keegan, R.M., Krissinel, E.B., Leslie, A.G.W., McCoy, A., et al. (2011).

Overview of the *CCP*4 suite and current developments. Acta Crystallogr. D *67*, 235–242. https://doi.org/10.1107/S0907444910045749.

55. Nurizzo, D., Mairs, T., Guijarro, M., Rey, V., Meyer, J., Fajardo, P., Chavanne, J., Biasci, J.-C., McSweeney, S., and Mitchell, E. (2006). The ID23-1 structural biology beamline at the ESRF. J. Synchrotron Radiat. *13*, 227–238. https://doi.org/10.1107/S0909049506004341.

56. Karplus, P.A., and Diederichs, K. (2012). Linking Crystallographic Model and Data Quality. Science *336*, 1030–1033. https://doi.org/10.1126/science.1218231.

57. Pace, C.N., and McGrath, T. (1980). Substrate stabilization of lysozyme to thermal and guanidine hydrochloride denaturation. J. Biol. Chem. *255*, 3862–3865. https://doi.org/10.1016/S0021-9258(19)85604-1.

STAR★METHODS

KEY RESOURCES TABLE

REAGENT or RESOURCE	SOURCE	IDENTIFIER
Chemicals, peptides, and recombinant proteins		
*Dr*BphP CBD	Takala et al. (2018)[18]	N/A
*Dr*BphP CBD-PHY	Takala et al. (2018)[18]	N/A
*Dr*BphP full-length	Kurttila et al. (2022)[24]	N/A
*Dr*BphP AtHK Chimera	Multamäki et al. (2021)[31]	N/A
Response regulator of *Dr*BphP (DrRR)	Multamäki et al. (2021)[31]	N/A
D-glucose (u^{13}C6, 99%)	Cambridge Isotope Laboratories	Cat# CLM-1396-PK
Ammonium Chloride (^{15}N, 99%)	Cambridge Isotope Laboratories	Cat# NLM-467-PK
Polyethylene glycol 3350	Sigma	Cat# 88776-250G-F
D-(+)-glucose anhydrous	MP Biomedicals LLC	Cat# 194672
D-($-$)-fructose	Sigma	Cat# F3510-1006
Ammonium acetate	Merck	Cat# 1.01116
Sodium citrate	Sigma-Alrdich	Cat# 51804-500G
Ethylene glycol	Sigma-Alrdich	Cat# 324558-100ML
Critical commercial assays		
QuickChange Lightning Multi Site-Directed Mutagenesis Kit	Agilent Technologies	Cat# 210513
Zn^{2+}-Phos-tag® SDS-PAGE assay	Fujifilm Wako Chemicals Europe GmbH	Ref# AAL-107S1
Deposited data		
Crystal structure of armless *Dr*BphP in Pr state	This paper	PDB code: 8BOR
Crystal structure of *Dr*BphP in Pr state	Takala et al. (2014)[12]	PDB code: 4O0P
Crystal structure of *Dr*BphP in Pfr state	Burgie et al. (2016)[14]	PBD code 5C5K
Experimental models: Organisms/strains		
E. coli BL21(DE3)	Thermo Scientific	Cat# EC0114
E. coli DH5α	Invitroge	Cat# 18265017
Oligonucleotides		
Armless mutants: 5′- TGG CTG CGG CCC GAA CTG CGG GGA GGA GGA TCC GGC TAC GCC GAG CCC TG -3′	This paper	N/A
Recombinant DNA		
pET21b(+) with *Dr*BphP CBD	Wagner et al. (2005)[47]	N/A
pET21b(+) with *Dr*BphP CBD-PHY	Wagner et al. (2007)[48]	N/A
pET21b(+) with *Dr*BphP	Wagner et al. (2007, 2008)[48,49]	N/A
pET21b(+) with *Dr*BphP AtHK Chimera	Multamäki et al. (2021)[31]	N/A
Software and algorithms		
MATLAB (R2022b)	MathWorks	https://se.mathworks.com/products/MATLAB.html
PyMOL Molecular Graphics System (version 2.0)	Schrödinger, LLC	https://pymol.org/2/
XDS program package (version Feb 5, 2021)	Kabsch (1993)[50]	https://www.esrf.fr/UsersAndScience/Experiments/MX/Software/PXSOFT/XDS/XDS_html_doc
Phaser (version 2.8.3.)	McCoy et al. (2007)[51]	https://www.phaser.cimr.cam.ac.uk/index.php/Phaser_Crystallographic_Software
Coot (version 0.9.6)	Emsley and Cowtan (2004)[52]	https://www2.mrc-lmb.cam.ac.uk/personal/pemsley/coot/
REFMAC5 (version 5.8.0352)	Murshudov et al. (2011)[53]	https://www2.mrc-lmb.cam.ac.uk/groups/murshudov/content/refmac/refmac.html
CCP4 interface (version 8.0.005)	Winn et al. (2011)[54]	https://www.ccp4.ac.uk

Structure
Article

CellPress
OPEN ACCESS

RESOURCE AVAILABILITY

Lead contact
Further information and requests for resources and reagents should be directed to and will be fulfilled by the Lead Contact, Janne Ihalainen (janne.ihalainen@jyu.fi).

Materials availability
This study did not generate new unique reagents.

Data and code availability
- The crystal structure of CBD-PHY armless is available in Protein DataBank (PDB ID: 8BOR). Any additional information required to reanalyze the data reported in this paper is available from the lead contact upon request
- This paper does not report original code.

EXPERIMENTAL MODEL AND STUDY PARTICIPANT DETAILS

The recombinant proteins used in this study were expressed in a pET21b(+) vector in *E. coli* BL21(DE3) cells as outlined in method details.

METHOD DETAILS

Cloning and DNA material
The pET21b(+) expression plasmids coding for wild-type *D. radiodurans* phytochrome fragments (CBD, CBD-PHY, full-length) were kindly provided by the laboratories of Prof. R. D. Vierstra and Prof. K. T. Forest.[5,48,47] The Chimera construct has the photosensory module of *Dr*BphP and the effector domain of phytochrome 1 from *Agrobacterium fabrum* (Agp1) as described in Multamäki et al. together with DrRR.[31] The 'arm' hairpin extension was clipped out by replacing segment between R446–G478 by a sequence "GGGS" with QuickChange Lightning Multi Site-Directed Mutagenesis Kit (Agilent Technologies) and confirmed by sequencing. The following primer, nonmatching sequence in italics, was used to mutate out the arm: 5' - TGG CTG CGG CCC GAA CTG CGG *GGA GGA GGA TCC* GGC TAC GCC GAG CCC TG - 3'.

Protein expression and purification
The protein constructs described above, with a C-terminal (His)$_6$-tag, were expressed in *Escherichia coli* BL21(DE3) at +28°C as described previously.[28] After lysis and ultracentrifugation, the purification was carried out with affinity chromatography followed by overnight incubation with 10x excess of biliverdin, and size-exclusion chromatography, where the samples were eluted with buffer (30 mM Tris pH 8.0), as described in Ihalainen et al.[28]

Crystallography
Crystals of the CBD-PHY armless were grown by hanging-drop vapor diffusion in dark at room temperature, after mixing 10 mg/mL protein at 1:1 ratio with reservoir solution (12% polyethylene glycol 3350, 200 mM ammonium acetate, 5% fructose, 5% glucose, and 100 mM sodium citrate pH 5.6). Crystal handling was conducted under green safe light. Once the first small flake-like crystals appeared within 3 weeks, they were used for seeding. There, the seed crystals were centrifuged, washed twice with a 1:1 mixture of the reservoir solution and buffer (30 mM Tris pH 8), and set to grow in 3 μL droplets in a fresh 1:1 mixture of reservoir solution and 10 mg/mL protein. After a month of crystal growth, the crystals were soaked with reservoir solution supplemented with 18% ethylene glycol, and flash-frozen.

Protein phosphorylation by acetyl phosphate and PhosTag detection
The PhosTag activity assay was adapted from Multamäki et al.[31] and performed as previously described.[24] The full-length (FL) and FL armless variants of *Dr*BphP were introduced with pre-phosphorylated response regulator from *D. radiodurans* (p-*Dr*RR). For this, *Dr*RR was phosphorylated at +37°C for 2.8 mg/mL of RR in the presence of 200 mM acetyl phosphate. Chimera and Chimera armless constructs were introduced with non-phosphorylated *Dr*RR. In the reaction, concentration of all phytochromes and *Dr*RR was 0.3 mg/mL. During a 5-min incubation at +25°C, the samples were pre-illuminated with saturating red LED (660 nm, 5 min, on average 13 mW/cm^2) or far-red laser (780 nm, Thorlabs, 20 s, 80 mW/cm^2) to reach the maximum Pr- or Pfr-state population, respectively. Once the (de)phosphorylation reactions were initiated with 1 mM ATP, the samples were incubated either under red light (as above) or in darkness at 25°C. After 10 min, the reactions were stopped with 5x SDS loading buffer. The mobility shift of phosphorylated RR (p-RR) proteins was detected using Zn^{2+}-PhosTag® SDS-PAGE assay (Wako Chemicals).

CellPress
OPEN ACCESS

Spectroscopic measurements

All measurements were performed in darkness and in ambient conditions (room temperature) unless otherwise stated. The samples were illuminated with 780 nm laser (ThorLabs) or 660 nm LED to drive them to either Pr or Pfr state, respectively.

UV-vis absorption spectroscopy

The steady-state UV-vis spectra were measured with a Cary 8454 UV/vis spectrometer (Agilent Technologies) in 10 mm Quartz cuvette right after saturating light conditions. After the background subtraction, the spectra were offset corrected at 850 nm and normalized to the 700 nm absorption in Pr state.

FTIR spectroscopy

The steady-state FTIR spectroscopy was performed using a Nicolet Magna IR-760 FTIR spectrometer with XT-KBr beam splitter, Ever-Glo IR source and MCT-detector. The measurements were conducted using 100 scans in the spectral range of 400–4000 cm^{-1} with a resolution of 2 cm^{-1}. Sample preparation and light-induced difference spectroscopy were performed as described in Takala et al.[18]

CD spectroscopy

The CD spectra were measured with Jasco J-715 CD spectrophotometer. The dark and illuminated spectra of the constructs were measured in 0.5 mm circular Quartz cuvette at 190–250 nm at 3–4 μM, and 250–800 nm at 0.27 mM sample concentration. For the illuminated spectra of CBD and the armless constructs, the spectra were measured in 300 nm wide sections, due to fast dark reversion of the systems (Figure S4). The samples were re-driven to the illuminated state between measurements, and four measurements per region were averaged.

The thermograms measured at 222 nm were concentration and heating rate dependent due to aggregation (Figures S9C and S9D). Therefore, the melting temperatures were determined in 10 mm cuvettes to allow lower concentration, but resulting in saturated spectra at wavelengths below 210 nm due to prominent $\Delta\epsilon$ of the Tris buffer. All measurements in far-UV region (210–250 nm) were performed in about 0.4 μM and in the near-UV-vis region (250–800 nm) in 8 μM concentration, unless otherwise stated. The 10-mm cuvettes also allowed the usage of Jasco PTC-348WI temperature control system with magnetic stirrer in the bottom during the temperature denaturation experiments. The $\Delta\epsilon$ at singular wavelength was recorded with 2°C intervals and the temperature was increased with 1°C/min heating rate. In the illuminated experiments, the sample was illuminated for 30 s between data points with a red LED mounted on the lid to prevent dark reversion.

QUANTIFICATION AND STATISTICAL ANALYSIS

Crystallographic data analysis

Diffraction data were collected at beamline ID23-1 of the European Synchrotron Radiation Facility (ESRF), Grenoble in 100 K with an X-ray wavelength of 1.07 Å,[55] and processed using the XDS program package version Feb 5, 2021.[50] The data were cut at 2.30 Å resolution, which corresponds to a correlation coefficient ($CC_{1/2}$) value of 0.325.[56] The CBD-PHY armless crystals belonged to space group P 1 2$_1$ 1 with four monomers in an asymmetric unit. The initial phases were solved with molecular replacement by using Phaser version 2.8.3.[51] The structure was further built and refined with Coot 0.9.6[52] and REFMAC5 version 5.8.0352,[53] and 0.01 matrix weight was applied for final refinement steps. The final structure had R_{work}/R_{free} values of 0.235/0.268. The electron density map for the figures was calculated from the final structure factor files with FFT of the CCP4 interface (version 8.0.005),[54] and the structure figures were created with the PyMOL Molecular Graphics System version 2.0 (Schrödinger, LLC). The crystal data collection and processing statistics are summarized in Table 1.

Spectroscopic data analysis

All spectroscopic data were analyzed and fitted, if need be, with Matlab version R2021b (The MathWorks, Inc).

The set of FTIR difference spectra (Pfr *minus* Pr and vice versa) were averaged together, offset corrected in the spectral range of 1981–1999 cm^{-1} and normalized to the negative D-ring C=O stretch signal at 1712 cm^{-1}.[28]

The temperature dependent data was used to determine melting temperatures. Decreasing T_m due to higher concentration, and vice versa, disclose that the T_ms do not result from monomerization of our homodimeric systems, and therefore the melting curves were fitted to unimolecular two-state model adapted from Greenfield[33] to determine the melting temperature T_m for the constructs:

$$K_{eq} = e^{\frac{\Delta H_{T_m} \cdot \frac{T}{T_m} - 1}{RT}},$$

(Equation 1)

where K_{eq} is the equilibrium constant, R is the gas constant, and ΔH_{T_m} is essentially the slope at the T_m. The fraction of unfolded protein can be also expressed as follows

$$F_u = \frac{K_{eq}}{K_{eq}+1},$$

(Equation 2)

Structure
Article

CellPress
OPEN ACCESS

where F_u is the fraction of unfolded protein. Finally, Equation 2 is combined with linear corrections to subtract contributions from linearly increasing or decreasing ellipticity.[57] If needed, the slope was fixed to a most frequent value determined in other cases.

$$f(T) = -F_u(T(S_f - S_u) - B_u + B_f) + (S_f \cdot T + B_f).$$ (Equation 3)